

Deep learning for intensity mapping observations: Component extraction

Kana Moriwaki^{1*}, Nina Filippova^{1,2}, Masato Shirasaki³, Naoki Yoshida^{1,5,6,7}

¹*Department of Physics, The University of Tokyo, 7-3-1 Hongo, Bunkyo, Tokyo 113-0033, Japan*

²*Department of Physics, Princeton University, Princeton, NJ 08544, USA*

³*National Astronomical Observatory of Japan (NAOJ), Mitaka, Tokyo 181-8588, Japan*

⁴*Kavli Institute for the Physics and Mathematics of the Universe (WPI), UT Institutes for Advanced Study, The University of Tokyo, 5-1-5 Kashiwanoha, Kashiwa, Chiba 277-8583, Japan*

⁵*Research Center for the Early Universe, School of Science, The University of Tokyo, 7-3-1 Hongo, Bunkyo, Tokyo 113-0033, Japan*

⁶*Institute for Physics of Intelligence, School of Science, The University of Tokyo, 7-3-1 Hongo, Bunkyo, Tokyo 113-0033, Japan*

ABSTRACT

Line intensity mapping (LIM) is an emerging observational method to study the large-scale structure of the Universe and its evolution. LIM does not resolve individual sources but probes the fluctuations of integrated line emissions. A serious limitation with LIM is that contributions of different emission lines from sources at different redshifts are all confused at an observed wavelength. We propose a deep learning application to solve this problem. We use conditional generative adversarial networks to extract designated information from LIM. We consider a simple case with two populations of emission line galaxies; $H\alpha$ emitting galaxies at $z = 1.3$ are confused with $[OIII]$ emitters at $z = 2.0$ in a single observed waveband at $1.5 \mu\text{m}$. Our networks trained with 30,000 mock observation maps are able to extract the total intensity and the spatial distribution of $H\alpha$ emitting galaxies at $z = 1.3$. The intensity peaks are successfully located with 74% precision. The precision increases to 91% when we combine 5 networks. The mean intensity and the power spectrum are reconstructed with an accuracy of $\sim 10\%$. The extracted galaxy distributions at a wider range of redshift can be used for studies on cosmology and on galaxy formation and evolution.

Key words: galaxies: high-redshift; cosmology: observations; large-scale structure of Universe

1 INTRODUCTION

Line intensity mapping (LIM) is a promising observational technique for next-generation cosmology. LIM probes the large-scale structure of the Universe at a wide range of redshift and thus enables us to study cosmology as well as galaxy formation and evolution (Kovetz et al. 2017). Fluctuations of the integrated intensity of emission lines such as Lyman- α , $H\alpha$, $[CII]$, and CO lines trace the distributions of the underlying galaxies, while hydrogen 21-cm line is used to study the distribution and ionization state of the intergalactic medium in the early Universe (Pritchard & Loeb 2012).

A number of LIM observation programmes have been proposed and are planned (see Kovetz et al. 2017). LIM measures the integrated emission from all the sources redshifted to a wavelength bin. While it provide rich infor-

mation on the sources and their large-scale distribution in principle, the confusion of sources or contamination from foreground/background emission is an inevitable problem in practice. Fonseca et al. (2017) show that multiple emission lines from galaxies often contribute roughly equally to the total intensity at a certain observed wavelength. There are a few methods to infer the contribution from a designated redshift. One is to perform cross-correlation analysis with other known tracers of galaxies or of the matter distribution at the same redshift (e.g. Visbal & Loeb 2010). More practical methods such as masking brightest pixels allow to detect subdominant signals (Gong et al. 2014; Silva et al. 2018). It is also possible to distinguish signals from different redshifts using the anisotropic power spectrum shapes (e.g. Cheng et al. 2016). These methods are aimed at estimating the statistical quantities, but do not generate direct images of the intensity distribution. It would be more informative and useful if contaminants are removed from an image to show explicitly the intensity distribution at an ar-

* E-mail: kana.moriwaki@phys.s.u-tokyo.ac.jp

bitrary redshift. Here, we propose to use deep learning to separate/extract information from intensity maps.

Convolutional neural networks (CNNs) are a popular and promising tool for image processing including problems related to LIM. Recent studies propose to use CNNs to analyse hydrogen 21-cm line signals from the epoch of reionization (Hassan et al. 2019; Hassan, Andrianomena & Doughty 2019; Gillet et al. 2019; Zamudio-Fernandez et al. 2019) or to estimate the line luminosity function from a CO intensity map (Pfeffer, Breyse & Stein 2019). Shirasaki, Yoshida & Ikeda (2019) use conditional generative adversarial networks (cGANs, e.g., Isola et al. 2016) to de-noise observed weak-lensing mass maps. A cGAN consists of a pair of CNNs that learn an image-to-image translation in an adversarial way, and is able to generate fine and complicated images.

In this letter, we apply cGANs to intensity maps to reconstruct the intensity distribution and basic statistics of galaxy distribution. We aim at decoding cosmological information from future intensity map observations using ground-based and space-borne telescopes. We show that our networks, after appropriately trained with a large set of mock observations, can generate accurately the intensity distribution from a single source population. Throughout this letter, we adopt Λ CDM cosmology with $\Omega_M = 0.316$, $\Omega_\Lambda = 0.684$, $h = 0.673$ (Planck Collaboration VI 2018).

2 METHODS

We consider the line intensity observed at wavelength of $1.5 \mu\text{m}$. Planned or proposed near-infrared LIM projects include the Spectrophotometer for the History of the Universe, Epoch of Reionization, and Ice Explorer (SPHEREx, Doré et al. 2016) and the Cosmic Dawn Intensity Mapper (CDIM, Cooray et al. 2019). Emission lines from galaxies at $z \sim 0-5$ are considered to be the dominant sources in this spectral regime. As a simple but realistic case, we assume that the observed line intensity map consists of two most dominant emission lines: $\text{H}\alpha$ line from $z = 1.3$ and $[\text{OIII}]$ 5007Å line from $z = 2.0$. Observational noises and other contaminants such as $[\text{OII}]$ 3727Å are to be considered in a forthcoming paper (Moriwaki et al. in preparation).

2.1 Mock intensity maps

We generate a number of mock intensity maps for training and testing in the following manner. First, we populate a cubic volume of $280h^{-1}$ Mpc with dark matter haloes using the publicly available PINOCCHIO code (Monaco et al. 2013). We set the minimum halo mass of the catalog to be $3 \times 10^{10}h^{-1} M_\odot$. We have tested and confirmed that the map properties such as the total line intensity are not significantly affected by this choice of the minimum halo mass.

We derive the halo mass-luminosity relation using the outputs of the cosmological hydrodynamics simulation Illustris-TNG (Nelson et al. 2019). We use the TNG300-1 dataset which has a simulated volume of $V_{\text{box}} = (302.6 \text{ cMpc})^3$. We compute the line luminosity from a simulated galaxy as

$$L_{\text{line}} = 10^{-A_{\text{line}}/2.5} C_{\text{line}}(Z) \text{SFR}, \quad (1)$$

where A_{line} accounts for attenuation by dust. We adopt

$A_{\text{H}\alpha} = 1.0$ mag and $A_{[\text{OIII}]} = 1.35$ mag. We use the photoionization simulation code CLOUDY (Ferland et al. 2017) to compute the coefficient $C_{\text{line}}(Z)$ as a function of the mean metallicity of the galaxy. The CLOUDY computation is done in the same manner as in Moriwaki et al. (2018) except that we adopt typical values of the electron density $n = 100 \text{ cm}^{-3}$ and the ionization parameter $U = 0.01$. We compute the luminosity of a simulated halo by summing up the luminosities of its member galaxies. The halo mass-luminosity relation, i.e., the mean \bar{L}_i and the variance σ_i within each halo mass bin, is then obtained from the Illustris output. To generate an emissivity field from a PINOCCHIO halo catalogue, we assume a Gaussian distribution with a mean \bar{L}_i and a variance σ_i and assign luminosities to the haloes in i -th mass bin.

We perform the above procedure for $\text{H}\alpha$ and $[\text{OIII}]$ independently at the respective redshift. We generate two-dimensional intensity maps by projecting the three-dimensional emissivity fields along one direction. The total area subtended by a map is $(3.4 \text{ deg})^2$, and we assume a spectral resolution $R = 40$ that corresponds to the expected resolution of SPHEREx. We find that the relative contribution from the $[\text{OIII}]$ emission (at $z = 2.0$) is $\sim 60\%$ of the $\text{H}\alpha$ map (at $z = 1.3$), which is consistent with other theoretical studies (Fonseca et al. 2017; Silva et al. 2018). To generate a large number of training data set, we use 300 different halo catalogues.

For each realization, 100 maps with an area of $(1.7 \text{ deg})^2$ are generated by projecting along random direction. We obtain 30,000 training data in total. In this way, we obtain training maps with various mean intensities. Each map has 256×256 pixels, corresponding to a pixel size of $(0.4 \text{ arcmin})^2$. For the test data set, we produce another 1,000 halo catalogs and generate 1000 independent maps. We smooth the training and test maps with a Gaussian beam with $\sigma = 1.2 \text{ arcmin}$ before giving them to the networks.¹

2.2 Convolutional networks

We construct cGANs based on PIX2PIX by Isola et al. (2016).² We train the networks so that they reconstruct both $\text{H}\alpha$ and $[\text{OIII}]$ images from an observed image. This kind of one-to-many image translation networks are studied by, for instance, Lee, Yang & Oh (2018) for separating transparent and reflection scenes.

We have two pairs of adversarial convolutional networks called generator and discriminator. They are denoted by (G_1, D_1) for $\text{H}\alpha$ map and by (G_2, D_2) for $[\text{OIII}]$ map. The generators try to reconstruct $\text{H}\alpha$ and $[\text{OIII}]$ maps from an observed map X_{obs} , whereas the discriminators try to distinguish the true maps $X_{\text{true},i}$ and the reconstructed maps $G_i(X_{\text{obs}})$. In other words, for an input (X_{obs}, X) with X being either $X_{\text{true},i}$ or $G_i(X_{\text{obs}})$, the discriminator returns a probability that X is $X_{\text{true},i}$. Here, $X_{\text{true},i}$ ($i = 1, 2$) denote the true maps of $\text{H}\alpha$ and $[\text{OIII}]$, respectively. The generator

¹ We have performed the same analysis in the present paper to the "raw" data without smoothing. We have found the performance of the cGANs is somewhat degraded when the networks are trained with the unsmoothed data populated with a number of discrete sources.

² <https://github.com/yenchenlin/pix2pix-tensorflow>

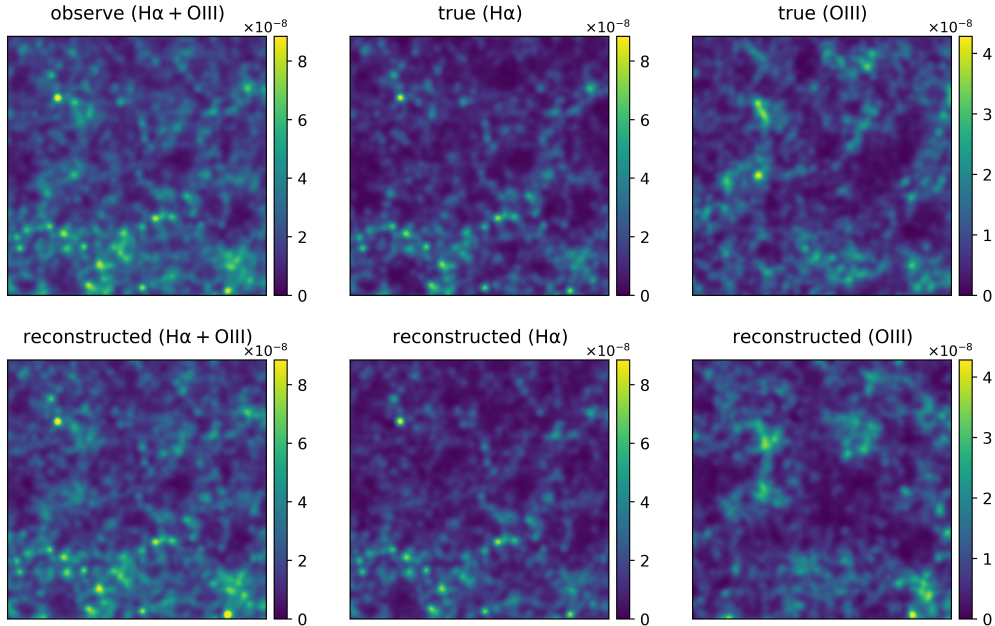


Figure 1. An observed map (top-left) is contributed by H α (top-center) and [OIII] (top-right) emission. The reconstructed H α and [OIII] maps and the sum of them are shown in bottom. The shown area is 1.7 deg on a side, and the intensities are in units of $\text{erg s}^{-1} \text{cm}^{-2} \text{sr}^{-1}$. Note the relative difference in intensity for H α and [OIII] (colour bars). Our network reconstructs even the fainter [OIII] component.

consists of 8 convolution layers followed by 8 de-convolution layers and the discriminator consists of 4 convolution layers. Two generators G_1 and G_2 share the first 8 convolution layers. The kernel size of the convolutions is 5×5 . In each layer, batch normalization,³ dropout, and skip connection are also performed (see Isola et al. 2016, for more details).

During the training phase, the performance of the generators and the discriminators are evaluated by a linear combination of the cross-entropy losses and the mean L1 norms:

$$\mathcal{L} = \sum_{i=1,2} [\mathcal{L}_{\text{cGAN}}(G_i, D_i) + \lambda_i \mathcal{L}_{\text{L1}}(G_i)] + \lambda_{\text{tot}} \mathcal{L}_{\text{L1,tot}}(G_1, G_2), \quad (2)$$

where

$$\mathcal{L}_{\text{cGAN}}(G_i, D_i) = \log D_i(X_{\text{obs}}, X_{\text{true},i}) + \log[1 - D_i(X_{\text{obs}}, G_i(X_{\text{obs}}))], \quad (3)$$

$$\mathcal{L}_{\text{L1}}(G_i) = \frac{1}{N_{\text{pix}}} \sum_{\text{map}} |X_{\text{true},i} - G_i(X_{\text{obs}})|, \quad (4)$$

$$\mathcal{L}_{\text{L1,tot}}(G_1, G_2) = \frac{1}{N_{\text{pix}}} \sum_{\text{map}} |X_{\text{obs}} - G_1(X_{\text{obs}}) - G_2(X_{\text{obs}})|, \quad (5)$$

where $N_{\text{pix}} = (256)^2$. In each training set, the generators (discriminators) are updated to decrease (increase) the loss function \mathcal{L} averaged over a mini batch.⁴ We adopt $\lambda_1 = \lambda_2 =$

$\lambda_{\text{tot}} = 100$ and a batch size of 4. The networks are trained for 8 epochs. We use the Adam optimizer (Kingma & Ba 2014) with learning rate 0.0002, and decay rate parameters $\beta_1 = 0.5$ and $\beta_2 = 0.999$ for updating the parameters.

3 RESULTS

3.1 Intensity reconstruction

We study the performance of our networks with 1000 test data. Fig. 1 shows an example of true and reconstructed maps. In our fiducial case of $\lambda_{\text{obs}} = 1.5 \mu\text{m}$, the contribution from H α is larger than [OIII], and then outstanding structures in the observed map mostly originate from the H α emission at $z = 1.3$. It is thus remarkable that not only the H α distribution but also the weaker [OIII] intensity is reproduced well.

It is important to study whether statistical quantities are also reproduced accurately. We first examine the peaks in our intensity maps. We select as "peaks" local maxima with heights greater than 3σ . We find 24089 (18859) and 24800 (17631) peaks in the true and the reconstructed H α ([OIII]) maps over our 1000 test data sets. Among them, 18262 (5095) peaks are matched correctly. This means that 76% (27%) of the true peaks are reproduced, and 74% (29%) of the reconstructed peaks are true.

If our purpose is to study individual peaks or other individual structures, we may require much higher accuracy for reconstructed structures. Previous studies developed cGANs

³ During test phase, we set `is_training = False` in batch normalization to use fixed normalization parameters.

⁴ Mini batch is a randomly selected set of training data, $\{X_{\text{obs},i}, X_{\text{true},i}\}_{i=0}^{n_b}$, where n_b is batch size. In training phase, the networks pass through all the training data without dupli-

cation. When we set the number of epochs $n_e > 1$, this passing through is repeated for n_e times. For n_d training data, updates are performed for $n_d n_e / n_b$ times in total.

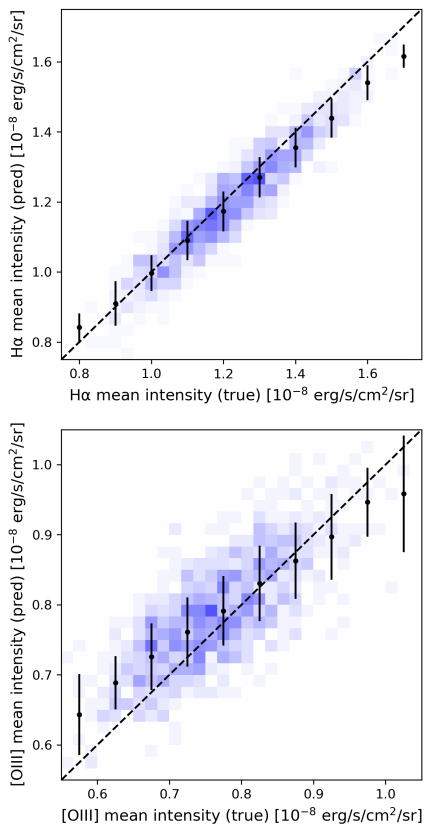


Figure 2. The mean intensities of the reconstructed maps against the mean of the true maps of H α (upper) and [OIII] (bottom) for our 1000 test data set.

that also learn the reliability of reconstructed maps (Lee, Yang & Oh 2018; Kendall & Gal 2017). In principle, we can use these methods to quantify the reliability of the outputs. Another promising idea is to combine multiple networks. To test this idea, we use 5 networks that have an identical set of convolutional layers but are trained with different sets of data. Intensity maps reconstructed by the 5 trained networks are similar, but not exactly the same. We find that it is generally difficult to reproduce the true intensity in portions where these networks commonly fail. For H α ([OIII]) maps, the number of peaks detected by all the 5 networks is 14332 (895). Among them, 13018 (539) peaks are true, which means a 91% (60%) confidence level for our peak detection. We note that if we take the average or the median of the reconstructed maps by multiple networks on a pixel-by-pixel basis, dark structures in void regions and small-scale structures are smoothed out.

3.2 Statistical information

Summary statistics such as the mean intensity and the power spectrum are primary tools to study the distribution and the properties of the emission-line galaxies. These can then be used for galaxy population studies or for cosmological parameter inference. In this section, we examine how well the mean intensity and the power spectrum are reconstructed.

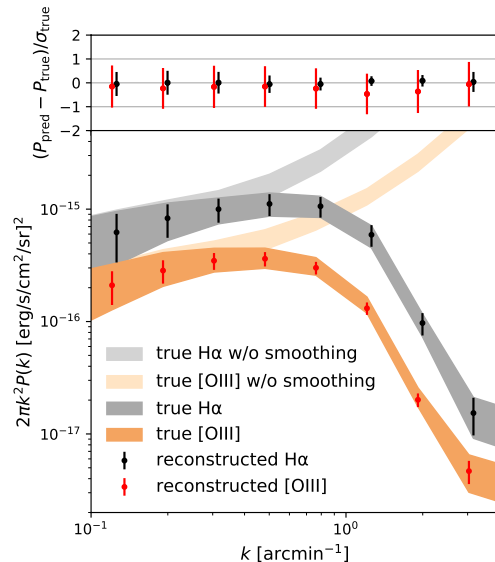


Figure 3. The two-dimensional power spectra of the reconstructed maps. The error bars and the shaded regions in the bottom panel show the 1σ variance of the power spectrum of the reconstructed and the true maps over 1000 test data, respectively. The light-coloured regions show the 1σ variance of true maps without smoothing. In the upper panel, we show the difference between the reconstructed and the true power spectra normalized by the variance of the true power spectrum.

We take medians of the reconstructed statistics by 5 different networks and compare them with true ones.

Fig. 2 shows the correspondence of the true and the reconstructed mean intensities. The mean intensities are widely distributed because of the cosmological variance of the underlying density field. We see clear correlations between the true and the reconstructed mean intensities. Fig. 2 shows that the mean H α ([OIII]) intensity of each $(1.7\text{ deg})^2$ map can be estimated with $\sim 10\%$ ($\sim 20\%$) accuracy. We note that the residual uncertainty is comparable to those resulting from the luminosity function estimates by recent galaxy surveys (Sobral et al. 2013; Khostovan et al. 2015). Planned LIM observations would have a much larger observational area. For instance, SPHEREx (Doré et al. 2016) will perform a deep survey over 200 deg^2 and thus the estimated mean intensities would have a much smaller statistical uncertainty.

We test if our networks generate accurate images (intensity maps) if the input observed map is significantly different from the training data. To this end, we input intensity maps with the mean differing as much as 20%. Some of these samples have mean intensities below or above the range plotted in Fig. 2. We find that the networks reconstruct the H α and [OIII] intensities with accuracy similar to those shown in Fig. 2 when both maps are scaled with the same factor. However, we find systematic offset when only one map is scaled more than 10% while the other being unchanged. In order to reconstruct these outliers accurately, we need to consider a wide variety of training data, and/or to combine multiple networks trained with maps in different mean intensity ranges.

Another important statistic is two-dimensional power

spectrum. Fig. 3 shows the variation of the true (shaded regions) and the reconstructed (error bars) power spectra. For reference, we also show the power spectra of unsmoothed true maps.⁵ Clearly, our networks *learn* the clustering of galaxies even though we do not explicitly teach that galaxies at different redshifts have different clustering amplitudes. The top panel of Fig. 3 shows the difference between the true and the reconstructed power spectra normalized by the square root of the variance of the true power spectra σ_{true} . We note that the variance of the training data is also σ_{true} . For H α map, the difference is typically less than σ_{true} at large scales; our network is able to recover the power spectrum of H α at $z = 1.3$ with an accuracy of $\sim 10\%$ from a confused map.

4 DISCUSSION

We have shown, for the first time, that cGANs can separate desired signals confused in an intensity map. We can also locate intensity peaks where emission line galaxies are clustered at the target redshift. Combining the distribution of the peaks and other information from follow-up observations of individual galaxies would allow us to study the environmental dependence of the galaxy formation.

A promising approach is to combine our deep learning method with other conventional method such as cross-correlation analysis. From the statistical information such as the power spectrum and the mean intensity of the reconstructed intensity maps (galaxy distributions) at a wide range of redshift, we can infer cosmological parameters and can also learn about the evolution of galaxy populations.

In this letter, we have presented the results from our first attempt, and there is much room for improvement. In order for our method to be applied to real LIM observations, the networks need to be trained with observational noises and other contaminants. For cosmology studies, it would be important to train the networks with a variety of astrophysical/cosmological models and parameters to improve robustness. Quantifying the uncertainty or the reliability of a reconstructed map is also important. When an input map is quite different from the training dataset, the networks should ideally return such information together with the reconstructed map(s). Methods shown in Kendall & Gal (2017) can be used for these purposes. To improve the ability of the networks, we can utilize the three-dimensional information or train the networks with a larger survey area/volume. Our networks can also be applied to observations in different wavelength such as sub-millimeter LIM. We choose two emission lines with relatively close redshifts having similar structures in this study. If one focus on two redshifts with larger separation, it could be easier for the networks to learn the difference and reproduce the maps well. We continue exploring the deep learning approach to, for instance, de-noise intensity maps or to extract designated information from a map with more than two components.

⁵ Power spectrum of the unsmoothed map $P(k)$ can be recovered from that of the smoothed map $P_{\text{sm}}(k)$ by $P(k) = \exp(k^2\sigma^2)P_{\text{sm}}(k)$, where σ is the smoothing scale of the Gaussian beam.

ACKNOWLEDGEMENTS

We thank the anonymous referee for providing us useful comments. We thank Yasuhiro Imoto for useful discussion. KM is supported by JSPS KAKENHI Grant Number 19J21379. NF's visit at the University of Tokyo was supported by the Princeton-UTokyo strategic partnership grant. MS is supported by JSPS Overseas Research Fellowships. NY acknowledges financial support from JST CREST (JPMHCR1414). A part of our computations in this study is carried out on Cray XC50 at Center for Computational Astrophysics, National Astronomical Observatory of Japan.

REFERENCES

- Cheng Y.-T., Chang T.-C., Bock J., Bradford C. M., Cooray A., 2016, *ApJ*, 832, 165
 Cooray A. et al., 2019, arXiv e-prints, arXiv:1903.03144
 Doré O. et al., 2016, arXiv e-prints, arXiv:1606.07039
 Ferland G. J. et al., 2017, *Rev. Mexicana Astron. Astrofis.*, 53, 385
 Fonseca J., Silva M. B., Santos M. G., Cooray A., 2017, *MNRAS*, 464, 1948
 Gillet N., Mesinger A., Greig B., Liu A., Ucci G., 2019, *MNRAS*, 484, 282
 Gong Y., Silva M., Cooray A., Santos M. G., 2014, *ApJ*, 785, 72
 Hassan S., Andrianomena S., Doughty C., 2019, arXiv e-prints, arXiv:1907.07787
 Hassan S., Liu A., Kohn S., La Plante P., 2019, *MNRAS*, 483, 2524
 Isola P., Zhu J., Zhou T., Efros A. A., 2016, *CoRR*, abs/1611.07004
 Kendall A., Gal Y., 2017, arXiv e-prints, arXiv:1703.04977
 Khostovan A. A., Sobral D., Mobasher B., Best P. N., Smail I., Stott J. P., Hemmati S., Nayyeri H., 2015, *MNRAS*, 452, 3948
 Kingma D. P., Ba J., 2014, arXiv e-prints, arXiv:1412.6980
 Kovetz E. D. et al., 2017, arXiv e-prints, arXiv:1709.09066
 Lee D., Yang M.-H., Oh S., 2018, arXiv e-prints, arXiv:1801.04102
 Monaco P., Sefusatti E., Borgani S., Crocce M., Fosalba P., Sheth R. K., Theuns T., 2013, *MNRAS*, 433, 2389
 Moriwaki K. et al., 2018, *MNRAS*, 481, L84
 Nelson D. et al., 2019, *Computational Astrophysics and Cosmology*, 6, 2
 Pfeffer D. N., Breyse P. C., Stein G., 2019, arXiv e-prints, arXiv:1905.10376
 Planck Collaboration VI, 2018, arXiv e-prints, arXiv:1807.06209
 Pritchard J. R., Loeb A., 2012, *Reports on Progress in Physics*, 75, 086901
 Shirasaki M., Yoshida N., Ikeda S., 2019, *Phys. Rev. D*, 100, 043527
 Silva B. M., Zaroubi S., Kooistra R., Cooray A., 2018, *MNRAS*, 475, 1587
 Sobral D., Smail I., Best P. N., Geach J. E., Matsuda Y., Stott J. P., Cirasuolo M., Kurk J., 2013, *MNRAS*, 428, 1128
 Visbal E., Loeb A., 2010, *J. Cosmology Astropart. Phys.*, 11, 016

Zamudio-Fernandez J., Okan A., Villaescusa-Navarro F.,
Bilaloglu S., Derin Cengiz A., He S., Perreault Levasseur
L., Ho S., 2019, arXiv e-prints, arXiv:1904.12846